Springer

KSME

Journal of Mechanical Science and Technology 28 (4) (2014) 1411~1420
www.springerlink.com/content/1738-494x
DOI 10.1007/s12206-014-0128-0

Experimental and numerical study of the load distribution in a ball-screw system †

Romuald Bertolaso[1], Mohammed Cheikh[2,*], Yoann Barranger[3], Jean-Christophe Dupré[3], Arnaud Germaneau[3] and Pascal Doumalin[3]

[1]*Université de Toulouse, Mines Albi, ICA (Institut Clément Ader), Campus Jarlard, F-81013 Albi cedex 09, France*
[2]*Université de Toulouse, IUT de Figeac, ICA (Institut Clément Ader), Avenue Nayrac, F-46100 Figeac, France*
[3]*Institut Pprime UPR 3346, CNRS - Université de Poitiers - ENSMA, 86962 Futuroscope Chasseneuil Cedex, France*

(Manuscript Received June 14, 2013; Revised October 10, 2013; Accepted November 13, 2013)

Abstract

In this work, load distribution on ball-screw systems (BSS) is determined by experimental techniques. Two optical techniques are used: photoelasticity for stress-field measurement and the mark-tracking method for displacement-field determination. In parallel to the experimental study, finite element method (FEM) and analytical solutions are used to calculate the loads applied on each ball of the BSS. Experimental results are used to validate the choice of boundary conditions and contact conditions between ball-screw and ball-nut in the FEM solution. The validation criterion is the correspondence between numerical and experimental fringes representing the differences of principal stresses. In addition to the study of load distribution, this paper presents the influence of the angle of contact direction on the stress distribution in BSS.

Keywords: Ball screw; Contact; Photoelasticity; Finite element method

1. Introduction

The objective of this work is the study of load distribution in a ball screw system (BSS). This system is a mechanical actuator usually used to translate the rotational motion of a screw to the linear motion of a nut. The friction between the nut and the screw is limited by the inclusion of balls and a re-circulation system during operation [1-3]. To study the life span of these systems, the load value applied on each ball needs to be identified. Several analytical solutions [4-6] are presented in the literature to attain this goal. Another way to find the load distribution at the ball-screw contact is to build a model using the finite element method (FEM) [7]. Both these approaches are based on hypotheses (geometry of contact, boundary conditions, friction model, etc.) and need experimental validation, which is indeed essential for any theoretical, numerical or technical solution to be qualified in aerospace applications.

To the best knowledge of the authors, there is no experimental study that presents a direct measurement of load distribution in a BSS. The manufacturers of these systems use an indirect process: after obtaining the load distribution by analytical or finite element methods, an endurance test is performed on the test bench. The fatigue criteria of the BSS are usually based on bearing fatigue laws. The load distribution is validated if the endurance limit criterion is not exceeded. Therefore, this approach does not allow contact forces and load distributions to be assessed directly.

To overcome the lack of experimental techniques for load distribution measurement in a BSS, non-contact methods can be used. Several optical techniques such as photoelasticity for stress-field measurement or digital-image correlation and the mark-tracking method for kinematics-field determination may be applied. An analysis can be carried out in 2D on the surface of the specimen [8, 9] or for a thin sample [10, 11] and in 3D in the bulk of volume [12-14] by using a tomography method like X-ray or an optical device.

The ball-screw system presents a complex geometry linked to the helical path of ball rolling. Furthermore, these contacts are local and distributed in the whole volume and the measurement of mechanical data is harder to perform in these particular zones. To avoid difficulties of implementation of 3D techniques and problems of accessibility, a simplification to two 2D problems is made: (1) a global study of a slice of specimen by neglecting the helix angle since the study is focused only on the mechanical behaviour in the vicinity of ball contact and the load distribution along the screw axis; (2) a local study of the contact angle in the case of a one-ball slice.

The present work is a first step in a global study of load distribution in a ball-screw system of trimmable horizontal stabiliser actuator (THSA) in an aircraft (Fig. 1). The movement of

*Corresponding author. Tel.: +33 5 65 50 30 77, Fax.: +33 5 65 50 30 61
E-mail address: mcheikh@univ-tlse2.fr
† Recommended by Associate Editor Seong Beom Lee

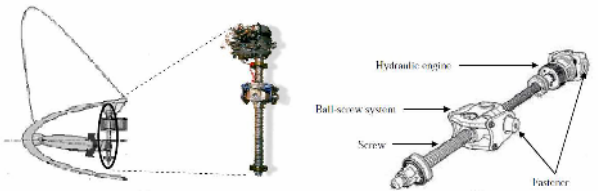

(a) (b)

Fig. 1. Ball screw system of the THSA plane.

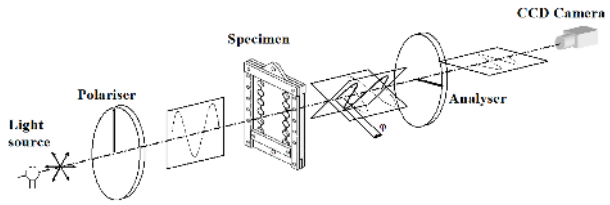

Fig. 2. Principle diagram of the photoelastic test.

a nut along a screw performs mobility of the back plane.

Firstly, a 2D finite element model is built, in order to calculate load distribution. Then, two measurement techniques, photoelasticity [10, 11] and the mark-tracking method [8, 15], are used to validate the FEM calculation. Experimental techniques make it possible to obtain an optimised mesh and realistic boundary conditions on a demonstrator specimen made in an elastic transparent material. The obtained FEM model remains viable in the elasticity domain whatever the material. Once the FEM modelling has been validated, the obtained load distribution and the contact angle evolution are compared to the results obtained by an analytical approach. The validated FEM solution can then be used to model the real 3D case using axisymmetric elements. The consideration of the helix angle is performed by post-processing of results obtained by FEM.

The next section presents the experimental and finite-element modelling of the global and local study on two demonstrators. The section also presents the analytical solution of load distribution in a BSS demonstrator. The last two sections present a discussion and a comparison between the experimental and numerical results obtained for both tests with an application example to an industrial case.

2. Methods

2.1 Measurement methods

Two experimental methods are used in this study: firstly photoelasticity is used to access the spatial stress distribution and secondly, the mark-tracking technique measures displacement in different locations of the specimens.

2.1.1 Photoelasticity

Photoelasticity is based on the optical-index properties of transparent materials, which yield data on stress distribution in the specimen model. The experimental setup used here is composed of a plane polariscope with an acquisition system (Fig. 2). The polariscope comprises a light source (white or monochromatic) and two polarising filters, called the polarised and the analyser. A specimen and a loading system are placed between these two filters. Under the phenomenon of birefringence, the specimen becomes optically anisotropic when loaded in that it has temporary double refraction. After traversing the sample, the wave is divided along two directions that correspond to the principal directions of the refractive index tensor. Through the analyser, the two waves propagate with the phase shift φ which is proportional to the difference of principal indexes. According to Maxwell Eqs. [16], this difference is linked to the principal stress difference:

$$\phi = \frac{2\pi Cd}{\lambda}(\sigma_1 - \sigma_2) \tag{1}$$

where d is the thickness of specimen, C is Brewster's constant and λ the wave length. The light intensity I recorded by CCD camera is given by the dark-field relationship [10, 11]:

$$I(x,y) = A^2 \sin^2(2\alpha)\sin^2\left[\frac{\phi}{2}\right] \tag{2}$$

with A a constant and α the angle between analyser and principal stress directions. The spatial distribution of I gives a two-fringe field: isochromatic and isoclinic fringes linked to α and φ respectively, *i.e.* intensity and direction of principal stresses.

2.1.2 Mark-tracking method

The mark-tracking method consists in determining the coordinates of the spot on the image at each load step. The coordinates (x_g, y_g) of one mark are given by the following Eqs. [8, 15]:

$$\begin{aligned} x_g &= \frac{\sum_{x=0}^{N_x}\sum_{y=0}^{N_y} x(f(x,y)-f_s)}{\sum_{x=0}^{N_x}\sum_{y=0}^{N_y}(f(x,y)-f_s)} + x_z \\ x_g &= \frac{\sum_{x=0}^{N_x}\sum_{y=0}^{N_y} x(f(x,y)-f_s)}{\sum_{x=0}^{N_x}\sum_{y=0}^{N_y}(f(x,y)-f_s)} + y_z \end{aligned} \tag{3}$$

where $f(x, y)$ is the grey level of the pixel of coordinates (x, y) and f_s is a lower limit used to extract the mark from the background (see Fig. 3). For example, for black marks, only pixels with intensity lower than f_s are taken into account in Eq. (3). The technique is used on a zone of interest defined around each spot by its upper left coordinates (x_z, y_z) and its size (N_x, N_y). For large deformations and movements, this search zone shifts automatically at each time step, taking into account the measured displacement, in order to keep the spot within the zone of interest. The threshold f_s is determined so that the mark size obtained in the process is the largest possible, while

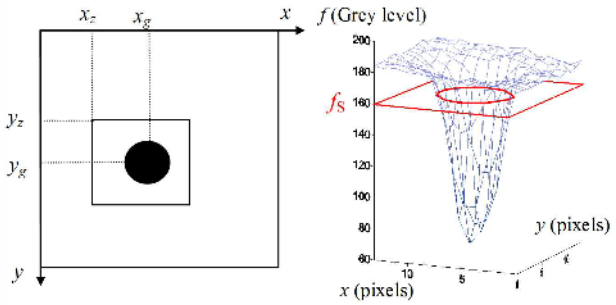

Fig. 3. Mark coordinates in mark tracking method.

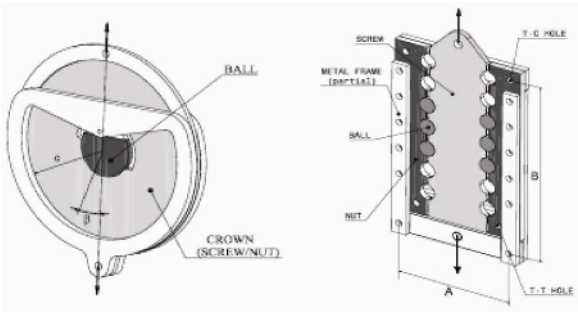

(a) Test B (b) Test A

Fig. 4. Diagram of specimens, A = 104 mm, B = 180 mm and C = 60 mm.

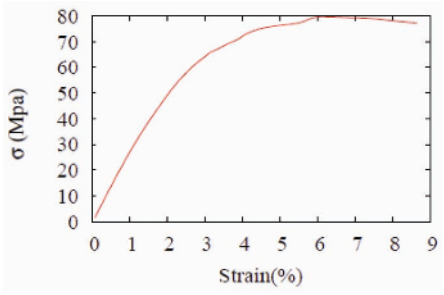

(a)

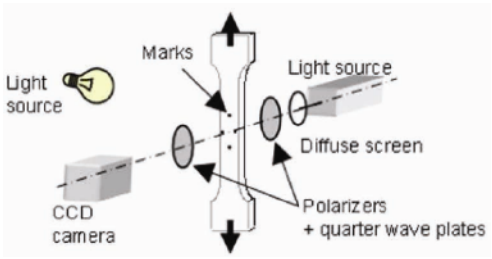

(b)

Fig. 5. (a) Material characteristic curve; (b) identification of photoelastic constant.

the background is discarded.

Accuracy is a function of the mark size: for a diameter greater than 8 pixels the tendency comes close to 0.025 pixels [15]. Finally, this technique gives the coordinates of each mark and its displacement by the difference in relation to the position in the initial image.

2.2 Demonstrator specimens

The specimen shown in Fig. 4(a) is the 2D simplified model of the ball-screw system (designated hereafter as **Test A**). The external dimension of the nut (dimension A in Fig. 4(a)) is A = 104 mm. The length of the BSS specimen (dimension B in Fig. 4(a)) is B = 180 mm. To analyse load distribution along the axial direction of the screw, the specimen may take up to seven rows of balls. The screw is loaded with its upper part always under tension and the load intensity is measured by a cell. The maximal applied load was chosen in order to maintain stress levels below the elastic limit of the material. For the nut, boundary conditions are imposed on the metal frame, which is assumed undeformable relative to the nut. The metal frame contains several holes for varying the type of limit conditions on the nut. One may have a T-T configuration (traction for screw and traction for the nut), or a T-C configuration (traction for the screw and compression for the nut). T-T configuration is obtained if the nut is attached to the frame at the bottom hole. T-C configuration is obtained if the nut is attached to the frame at the upper hole. An intermediate configuration between T-T and T-C can be obtained if the intermediate holes are used.

To observe the stress evolutions at the contact zone, the second assembly is used (designated hereafter as **Test B**), as shown in Fig. 4(b). The diameter of the crown representing the screw or the nut is 120 mm and the diameter of the ball is 35.72 mm. The influence of the contact angle β can be studied by rotating the crown, which represents the nut or the screw, around the ball from 0° to 60°. The groove of this assembly has a gothic geometry comprised of two semi-circles, giving a shape close to the real one of the BSS groove.

Specimens are made in PMMA material with a thickness d = 5 mm. Mechanical properties and Brewster's constant are determined simultaneously with a tensile device placed in a polariscope (Fig. 5) [17]. Young modulus, Poisson coefficient and photoelastic coefficient are equal to E = 2.25 GPa, ν = 0.3 and C = 60 Bw, respectively.

2.3 FEM modelling

Specimens were meshed by linear 2D elements with refined zones around the contact areas as shown in Figs. 6 and 7. These meshes are obtained by ZéBuloN finite element code (*one can see www.numerics.com for more information about this code*). The specimen of **Test A** was meshed by 52161 elements and 51369 nodes hence 102738 Degrees Of Freedom. For the contact zone, the C2D4 quadrangle elements with four nodes are used and the C2D3 triangular elements with three nodes are used for the remains of the mesh. Given the symmetry of the specimen geometry and the applied loading, only half of the system was modelled. The boundary condition of **Test A** are presented in Fig. 6. Blocking was applied along x

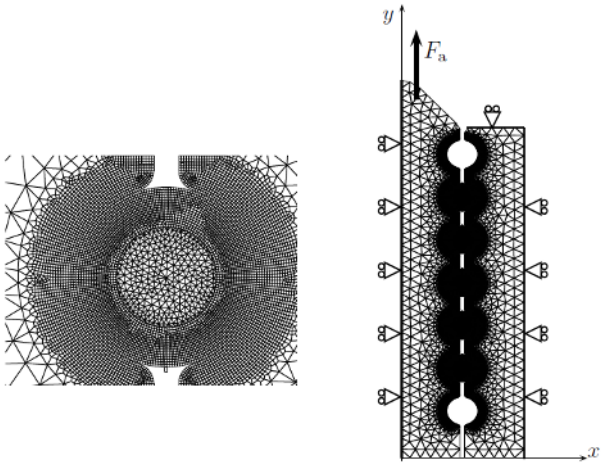

Fig. 6. Specimen 2D mesh of the ball screw system (Test A) with zoom on the ball and boundary conditions.

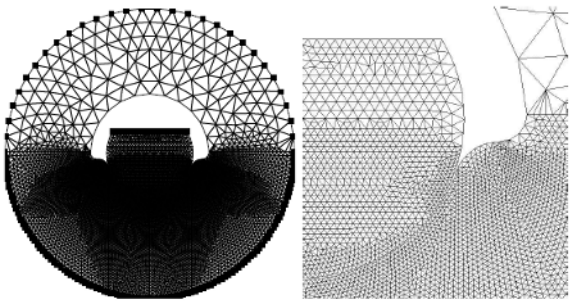

Fig. 7. Specimen 2D mesh of the Test B with a zoom in the right contact zone.

axis of the screw to represent the state of symmetry condition of the set. The load was applied on the top of the screw as an imposed displacement.

Blocking along the *x* axis was imposed on the right edge of the nut to model the radial stiffness of the system. To model the T-C configuration of the system, the screw top edge was blocked along the y axis. For **Test A**, two simulations were performed: one with a nominal geometry with ball diameter constant and equal to 7.144 mm. Then a second simulation was carried out, taking into account the dimensional errors of the ball diameters [18] induced by machining. Radius errors were -0.004 mm, -0.025 mm and -0.0125 mm on the lower three balls respectively. The same mesh and the same boundary conditions were used for both simulations.

The specimen of **Test B** was meshed by 19414 elements and 9930 nodes hence 19860 DOFs. The C2D3 triangular element with three nodes is used for this mesh. For this test, the load is applied on the top of the ball along the *y* axis (vertical axis of the view) and the crown was clamped at its end. Variation of β was imposed by turning the crown simulating the nut or screw. Two calculations were performed for this test, corresponding to two angles of contact direction (β = 0° and β = 40°).

Table 1. Mechanical characteristics of the specimens material (PMMA) used in simulation.

Young's modulus (GPa)	210
Poisson's ratio	0.3
Thickness (mm)	5

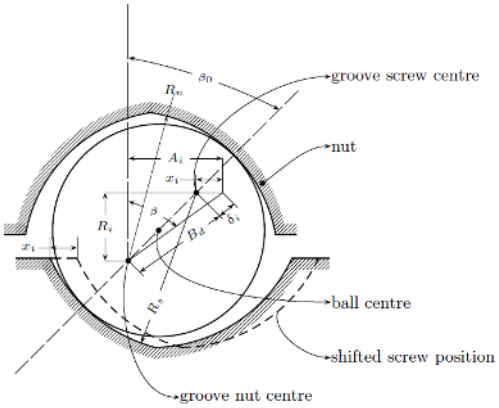

Fig. 8. Geometrical relationship between centres of grooves and ball centre.

Given the low thickness of the specimens, the calculation was performed using the plane-stress hypothesis. The material used was PMMA, whose characteristics are presented in Table 1. Balls-screw contact and balls-nut contact were taken into account by using Lagrange multipliers with friction coefficient of μ = 0.4 [19]. All calculations in this study were performed with *ZéBuloN* computer code [20].

2.4 Analytical approach

The proposed analytical solution is an adaptation of the Jones method of calculating load distribution in bearings [21] applied to the BSS specimen used in this study. Fig. 8 presents the geometrical relationship between the centre positions of the screw groove and the nut groove with the centre of the ball. In the absence of a radial load and an axial preload for the studied case, the contact happens at two points only, despite the gothic shape of the groove. The equation of the contact angle is given by [22]:

$$\sin \beta_i = \frac{A_i}{B_d + \delta_i}. \tag{4}$$

δ_i is the crushing balls under the influence of the contact pressure. B_d is the distance between the groove centres of screw and nut. This distance is obtained by $B_d = (f_n + f_s - 1)D_b$ with D_b the ball diameter, $f_n = R_n/D_b$ and $f_s = R_s/D_b$. R_n and R_s are the radii of screw and nut grooves, respectively. Ball crushing δ_i is related to the contact pressure by Hertz's relation [23]:

$$\delta_i = CP_i^{\frac{2}{3}} \tag{5}$$

with $C = C_s + C_n$. These two parameters C_s and C_n represent the hertzian contact stiffness between balls and screw and between balls and nut respectively. For each ball of the system, one can deduce the geometrical relationship from the Pythagorean theorem:

$$\delta_i = (A_i^2 + R_i^2)^{\frac{1}{2}} - B_d \,. \tag{6}$$

Parameters A_i are related to the displacement xi by:

$$x_i = A_i - B_d \sin\beta_0 \,. \tag{7}$$

Radial deformations of the system are negligible and the R_i parameter is a constant. x_i is the shift of the centre of the screw groove to the centre of the nut groove. Extending $x_i - x_{i-1}$ of a portion of the screw can be deduced from the geometric relationship of the figure:

$$x_i - x_{i-1} = A_i - A_{i-1} \,. \tag{8}$$

In the studied case, the extremities of the nut are embedded and the system extension is due only to the longitudinal extension of the screw.

$$x_i - x_{i-1} = \frac{F_i L}{ES} \tag{9}$$

where L is the pitch of the screw, E is the Young's modulus and S the cross section of the screw. Force F_i is the internal force of the screw at the ball i. For T-C configuration, internal forces F_i are related to external forces F_a by the relation:

$$F_i = F_a - \sum_{j=1}^{i-1} P_j \sin\beta_j \,. \tag{10}$$

The combination of Eqs. (4), (5), (8), (9) and (10) gives [4]:

$$K\left(F_a - \sum_{j=1}^{i-1} P_j \frac{A_j}{B_d + CP_j^{\frac{2}{3}}}\right) = A_{i-1} - A_i \tag{11}$$

with $K = L/(ES)$. Taking into consideration Eq. (4), the balance of external forces with ball load is expressed by [5]:

$$F_a = \sum_{j=1}^{n} P_j \frac{A_j}{B_d + CP_j^{\frac{2}{3}}} \tag{12}$$

with n the number of balls in the system.

Eqs. (6), (11) and (12) represent $2\times n$ nonlinear equations to solve. Newton Raphson's method is used to solve this system. Resolution of this system allows the identification of the load distribution P_i and the contact angles β_i using Eq. (4) and parameters A_i.

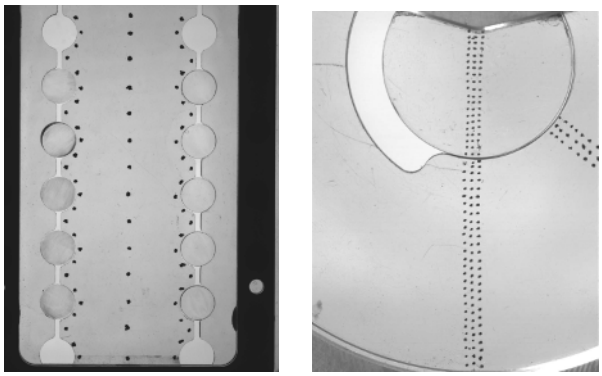

(a) Test A (b) Test B

Fig. 9. PMMA specimens with marks.

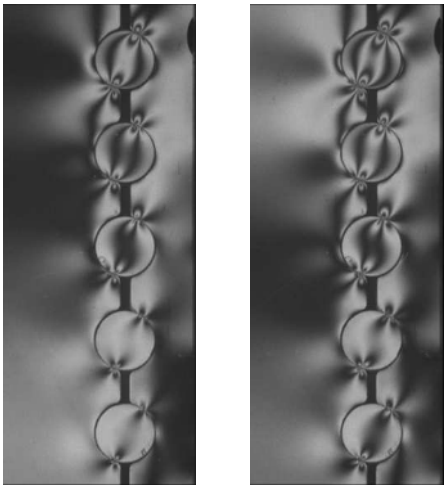

(a) F_a = 240 N (b) F_a = 318 N

Fig. 10. Experimental isochromatic fringes.

3. Results

3.1 Validation of numerical models by experimental data

Photoelasticity gives the experimental fringes. From finite element results, simulated fringes are calculated by using Eqs. (1) and (2) from the stress tensor. The comparison between experimental and numerical fringes is then performed. Furthermore, displacements measured by the mark-tracking method are compared to those obtained by simulation. Marks are plotted along axis of the screw for **Test A** (Fig. 9(a)) and along load direction axis for **Test B** (Fig. 9(b)). Therefore the confrontation is double from both static (stress) and kinematics (displacement) fields, which then allows validation of the simulation hypotheses.

3.1.1 Test A: distribution of load along the BSS

Fig. 10 shows the experimental isochromatic fringes of the right side of specimen with five rows of balls. Figs. 10(a) and (b) present the load cases of F_a = 240 N and F_a = 318 N, respectively. In the test beginning at low load, ball/screw and ball/nut contacts appear on the first row of balls. Contacts

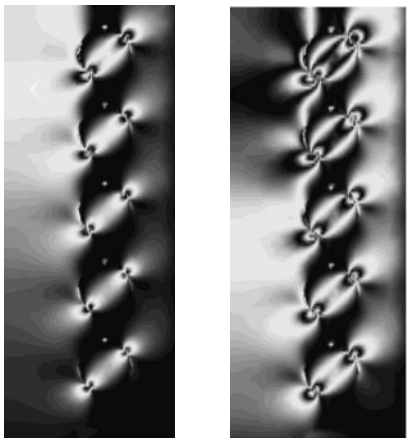

(a) F_a = 240 N (b) F_a = 318 N

Fig. 11. Simulated isochromatic fringes for nominal geometry.

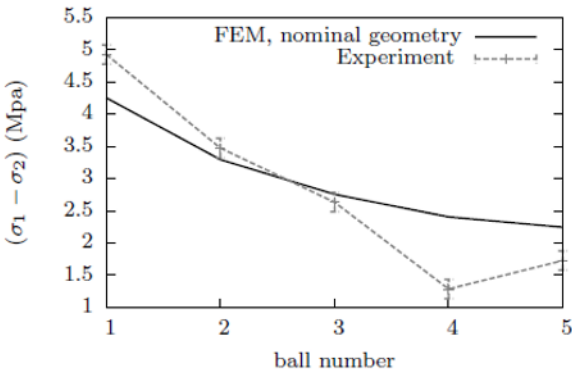

Fig. 12. Principal stress difference distribution for the first simulation with nominal geometry and Fa = 318 N.

appear on the other rows of balls by increasing the load intensity with upper balls being the most heavily loaded. Two contact points appear on each ball, highlighted by fringe concentration zones. The evolution of the fringes is symmetrical with respect to the screw axis regardless of the applied load. The density of fringes decreases with ball position, which corresponds to the decrease in contact stress intensity with the distance to the applied load point.

Simulated fringes obtained by Eq. (2) are presented in Fig. 11 for the first simulation corresponding to the nominal geometry (without dimensional error of balls). This figure presents two load cases corresponding to the experimental case, hence F_a = 240 N and F_a = 318 N. Qualitatively, distributions of simulated fringes are similar to those found in the experiment. The same distribution pattern of fringes is observed in experimental and numerical results. The first row (upper ball on Fig. 11) is the most heavily loaded. The two contact points on each ball give directions and the angle contact β for each ball. The number of fringes and therefore, the stress levels in the case of a load of F_a = 318 N is greater than in the case of a load of F_a = 240 N. Nevertheless, from a quantitative viewpoint, a discrepancy between experimental and numerical

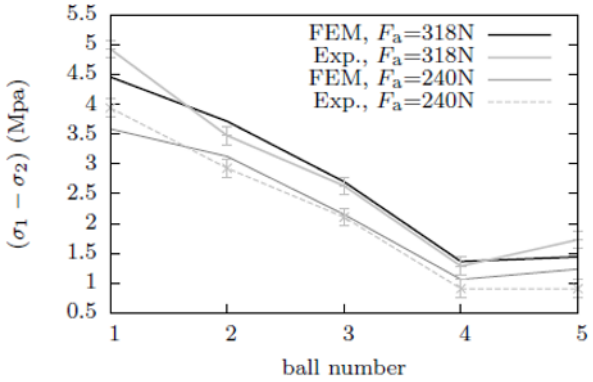

Fig. 13. Principal stress difference distribution for the second simulation with corrected radii errors for F_a = 240 N and F_a = 318 N.

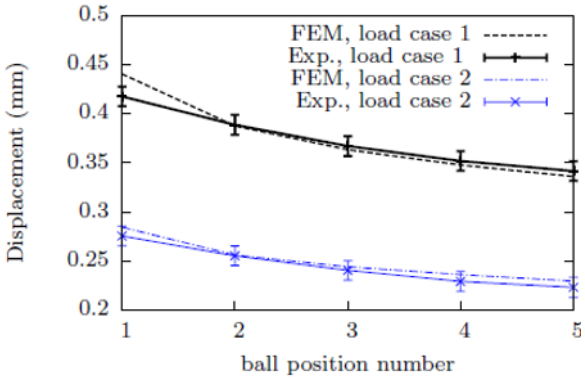

Fig. 14. Mark displacement evolution for Test A.

results is observed for the first simulation with nominal geometry. Fig. 12 shows the principal stress difference (σ_1-σ_2) versus the number of balls obtained by experiment and by FEM. Experimental (σ_1-σ_2) are obtained by experimental fringes and Eq. (1) with sin $\varphi/2 = 0$. The evolution tendency of (σ_1-σ_2) is the same for both simulation and experiment. The upper row of ball is the more heavily loaded and the bottom row is the least loaded. However, the numerical values differ between simulation and experiment especially for balls 5 and 6. This difference is due to the geometrical errors induced by the machining process.

Fig. 13 shows the principal stress difference values for load case F_a = 318 N and F_a = 240 N for the second simulation. In this simulation, errors on the ball radii are corrected as was indicated in Sec. 2.3. This figure shows good agreement between simulation and experiments. Small differences noticed in the figure are due mainly to machining errors of the nut and screw. These results clearly show the influence of dimensional errors on the load distribution in a BSS, as has been discussed in Ref. [24] by Mei et al.

The results obtained experimentally by the mark-tracking method and by FEM are shown in Fig. 14. The load cases are selected according to the level of displacement of the central row of balls (third ball). The load cases correspond to a displacement of 0.37 mm for load case 1 and 0.24 mm for load

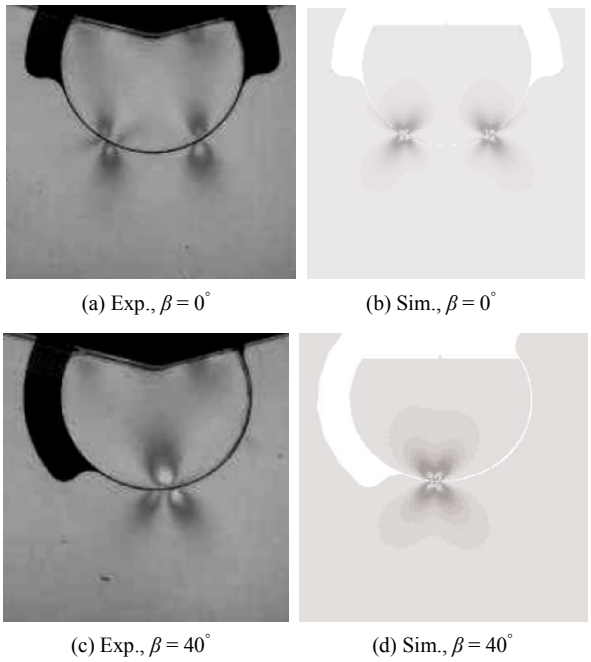

(a) Exp., $\beta = 0^{\circ}$ (b) Sim., $\beta = 0^{\circ}$

(c) Exp., $\beta = 40^{\circ}$ (d) Sim., $\beta = 40^{\circ}$

Fig. 15. Experimental and FEM fringes for Test B with Fa = 50N.

case 2. Fig. 14 shows the evolution of longitudinal displacement U_x of the screw axis marks shown in Fig. 9(a). The position of the each ball corresponds to the position of the mark. This figure shows a good correspondence between the solutions obtained by FEM and by experiment. The small differences observed between simulation and experiment are of the order of 2 percent for the first row of balls.

3.1.2 Test B: local contact

Experimental results of **Test B** are presented in Fig. 15. This figure shows experimental and simulated photoelastic fringes for two contact direction angles $\beta = 0°$ and $\beta = 40°$ with $F_a = 50$ N. There is a good correspondence between experimental and numerical results. For $\beta = 0°$ (Figs. 15(a) and (b)), two contact points are shown symmetrical about axis y (the central axis of the ball). The presence of two contact points is justified by the crown's gothic shaped groove. If the contact direction β increases, only one contact point remains with a higher number of fringes describing a higher stress value as shown in Figs. 15(c) and (d).

Fig. 16 presents the evolution of experimental and simulated displacements along the load direction according to the mark positions shown on Fig. 9(b). Marks with $x \leq 40$ mm belong to the crown and marks with $x > 40$ mm belong to the ball. There is a good correspondence between both approaches. A jump in displacement around the 40 mm position is observed. This jump is due to non contact of the ball with the crown along the observation line; so the displacement field cannot be continuous. The height of the jump is higher for $\beta = 0°$ than $\beta = 40°$ since the observation line is closer to the contact point.

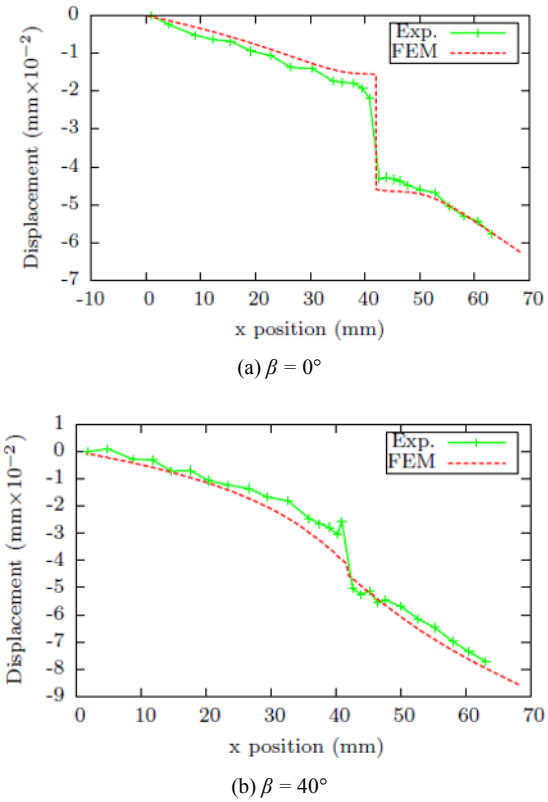

(a) $\beta = 0°$

(b) $\beta = 40°$

Fig. 16. Mark displacement evolution for Test B.

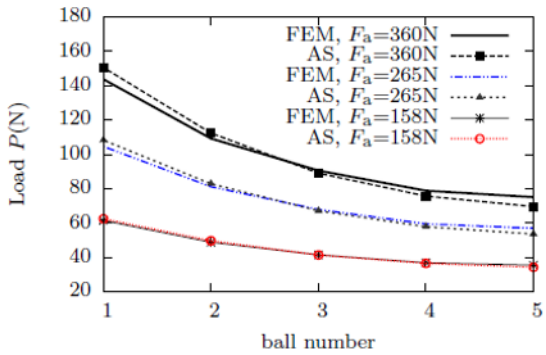

Fig. 17. Load distribution versus ball number position for FEM and analytical solution (AS).

3.2 Comparison between analytical and numerical results

The analytical solution presented in Sec. 2.4 allows calculation of contact loads P_i, contact angles β_i, axial displacement x_i and the ball crushes δ_i of the BSS presented in Section 2.3. This analytical solution will be possible after resolution of the 10 nonlinear Eqs. (11) and (12) by the Newton-Raphson method.

It should be noted that the analytical solution neglects the radial deformation of the system. Load distribution P_i, as well as the other unknowns, β_i and δ_i depend only on the axial deformation x_i of the screw.

Fig. 17 shows the evolution of contact forces P_i obtained by

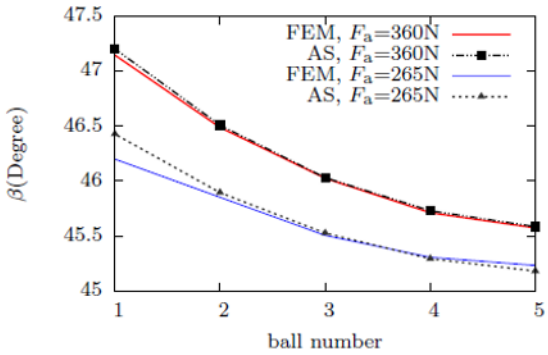

Fig. 18. Evolution of contact angle β versus ball number position.

FEM and by analytical solution (AS) for three load cases: F_a = 360 N, F_a = 265 N and F_a = 158 N. These analytical and numerical results clearly show that the first row of ball is the more heavily loaded and the ratio of the contact forces between the first and last rows of balls is practically 2 for the three load cases. A similar pattern for the contact angle is observed in Fig. 18. The contact angle decreases away from the point of load application.

4. Discussion

The FEM solution has been validated from a static viewpoint by the photoelasticity technique and kinematically by the mark-tracking method. The analytical solution showed that distribution of loads depends primarily on the axial deformation of the BSS. However, in order that the FEM solution may be applied to an industrial case, three corrections must be made: system modelling should be done using a metallic material and not with PMMA; cylindrical shape should be used for the system and not a flat one; finally, the helix angle should be taken into account.

In this study, it is assumed that the material is linear elastic, and so the value of Young's modulus and Poisson's ratio should not influence the load distribution. The solution thus remains valid for a metallic material. The cylindrical form of the system can be taken into account by selecting axisymmetric finite elements. Indeed, the same mesh used for the PMMA study will be used for industrial case simply by changing 2D elements to axisymmetric elements. The accuracy of the mesh will not then be affected.

The helix angle in the analytical and FEM models is considered equal to zero Degree. Analytical and finite element solutions remain valid at the near multiplicative coefficient cos γ. To take into consideration the helix angle, one simply multiplies the forces P_j in Eqs. (10) and (12) by cos γ, hence [24]:

$$F_i = F_a - \sum_{j=1}^{i-1} P_j \cos\gamma \sin\beta_j \tag{13}$$

Table 2. Geometric and mechanical characteristics of the industrial BSS.

R_b (mm)	R_s (mm)	R_n (mm)	L (mm)	γ	E (GPa)	v	m	r
7.144	28.5	29.	22.	7°	210.	0.3	12	5

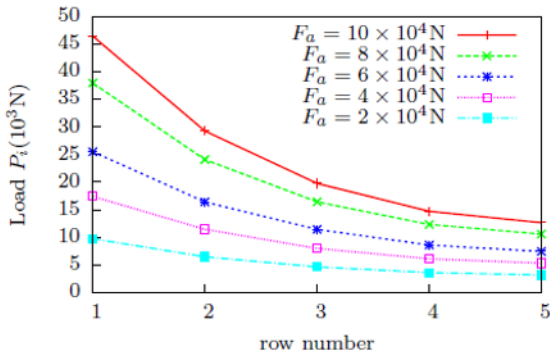

Fig. 19. Forces contact evolution P_γ versus the row number for the industrial case.

and

$$F_a = \sum_{j=1}^{n} P_j \cos\gamma \frac{A_j}{B_d + CP_j^2}. \tag{14}$$

For the FEM solution, the helix angle can be taken into account by postprocessing. In this case, contact force P_γ^i of each row ball is obtained by :

$$P_\gamma^i = \frac{P_i}{\cos\gamma} \tag{15}$$

with γ obtained from BSS geometry [25]:
$\gamma = \arctan(L / 2\pi R_s)$ and P_i the contact forces obtained by FEM.

The evolution of contact forces on different balls is defined by:

$$P_n^i = \frac{P_\gamma^i - P_\gamma^{i-1}}{mL^2} n + p_{n-1}^i \tag{16}$$

with n the ball number in the row i, m the total number of balls by row. For the last row, the least loaded row, the contact force for each ball is defined by $P^i = P_\gamma^i / m$ and not by Eq. (16). For each row, one considers that $P_0^i = p_m^{i-1}$.

By way of application, the results for an industrial BBS, whose geometry corresponds to demonstration model presented in Sec. 2.2 in configuration T-C, are presented bellow. The mechanical and geometric characteristics of the industrial BSS are summarised in Table 2. Fig. 19 shows the load distribution versus the row number for 5 load cases from 20 kN to 100 kN with helix angle of γ = 7°. For the maximal load case

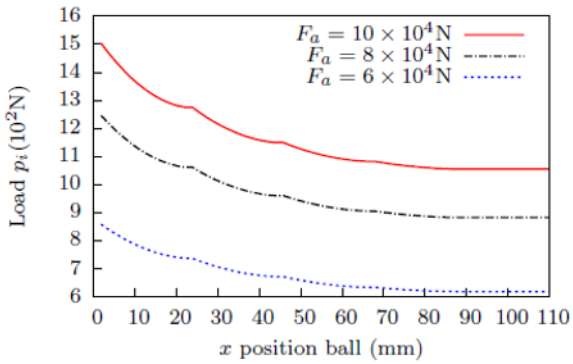

Fig. 20. Ball forces contact evolution p versus the ball position for the industrial case.

F_a= 100 kN, the contact force at the first row of balls reaches $P_\gamma^1 = 51.37$ kN, while the last row is only $P_\gamma^5 = 14$ kN.

Fig. 20 shows the trend of contact forces on each ball for 3 load cases in the industrial case. These values will be used in the fatigue laws of the BSS to calculate their lifespan.

5. Conclusions

In this work, the load distribution in a ball-screw system is studied by three approaches: analytical, numerical and experimental. The latter has been used to validate the first two approaches. In order to assess stress distribution in the BSS, in particular at the different contact points, a photoelasticity test bench was used. The results show that the row of balls closest to the point of load application is the most stressed. The value of the loads on the balls reveals a continuing decrease the further away one gets from that point of loading. Discussions in the previous section showed that a 2D FEM model, experimentally validated, can be used for an industrial case using axisymmetric elements. This study focuses on the 2D case. Further work is underway to complete the study in a 3D case with adapted experimental volume measurement methods [14, 26].

Acknowledgment

This study is sponsored by Conseil Régional Midi-Pyrénées (CRMiP) and Ratier Figeac. The authors wish to thank M. Malvy President of CRMiP for his support for the growth of research activities at the Figeac IUT and E. Delbos (of Ratier Figeac) for the helpful discussions and granting permission for publication. The authors are grateful to A. Fermy (of Figeac IUT) for the manufacturing of the specimens used in the experimental section of this work.

References

[1] C. C. Wei and R. S. Lai, Kinematical analyses and transmission efficiency of a preloaded ball screw operating at high rotational speeds, *Mechanism and Machine Theory*, 46 (7) (2001) 880 - 898.

[2] D. Mundo and H. S. Yan, Kinematic optimization of ball-screw transmission mechanisms, *Mechanism and Machine Theory,* 42 (1) (2007) 34-47.

[3] J. Y. Liu, M. H. Hsu and F. C. Chen, On the design of rotating speed functions to improve the acceleration peak value of ball-screw transmission mechanism, *Mechanism and Machine Theory,* 36 (9) (2001) 1035-1049.

[4] T. Yasuyoshi, Y. Takafumi and M. Susumu, Study on load distribution and ball motion of a ball screw, *Journal of Japonese Society of Tribologist*, 48 (2003) 659-666.

[5] H. Shimoda, Stiffness analysis of ball screws: influence of load distribution and manufacturing error, *Int. J. Japan Soc. Prec. Eng.*, 33 (1999) 168-172.

[6] T. Huang and B. Ravani, Contact stress analysis in ball screw mechanism using the tubular medial axis representation of contacting surfaces, *Journal of Mechanical Design*, 119 (1) (1997) 8-14.

[7] P. Matt, *Développement de nouveaux codes de calcul de durée de vie de vis à billes*, Rapport des travaux RF 5664-99, Ratier-Figeac, Figeac, France (1999).

[8] J. S. Sirkis and J. T. Lim, Displacement and strain measurement with automated grid methods, *Experimental Mechanics*, 31 (4) (1991) 381-388.

[9] M. Bornert, F. Brémand, P. Doumalin, J.-C. Dupré, M. Fazzini, M. Grédiac, G. Hild, S. Mistou, J. Molimard, J. J. Orteu, L. Robert, Y. Surrel, P. Vacher and B. Wattrisse, Assessment of digital image correlation measurement errors: Methodology and results, *Experimental Mechanics*, 49 (3) (2009) 353-370.

[10] E. A. Paterson and Z. F. Wang, Towards full field automated photoelastic analysis of complex components, *Strain*, 27 (1991) 49-56.

[11] A. Lagarde, N. Plouzennec, J. C. Dupré, Determination of isoclinic and isochromatic parameters by photoelastic and numerical analysis. In *3rd Biennal European Join Conference on Engineering Systems Design and Analysis (ESDA),* Montpellier, France, 1-4 July (1996).

[12] A. Lagarde, A. Zenina, J. C. Dupré, Separation of isochromatics and isoclinics patterns of a slice optically isolated in a 3d photoelastic medium, *European Journal of Mechanics*, 18 (1999) 633-640.

[13] A. Germaneau, F. Peyruseigt, S. Mistou, O. Dalverny, P. Doumalin and J. C. Dupré, Experimental validation of a spherical plain bearing numerical model by scattered light photoelasticity, *J. Engineering Tribology* (2008) 647-656.

[14] Y. Barranger, *Apport des méthodes volumiques dans la confrontation théorie/expérience : application à la rupture fragile et aux contacts conformes*, Thèse universitaire, Université de Poitiers, France (2010).

[15] N. Bretagne, V. Valle and J. C. Dupré. Development of marks tracking technique for strain field and volume variation measurements, *NDT&E Int*, 38 (2005) 290-298.

[16] A. S. Kobayashi, *Handbook on Experimental Mechanics*,

Prentice-Hall, (1987).
[17] P. Doumalin A. Germaneau and J. C. Dupré, 3D photoelasticity and digital volume correlation applied to 3D mechanical studies. In *Proc. ICEM 13*, Greece (2007).
[18] J. Liu, Y. Shao and T. C. Lim, Vibration analysis of ball bearings with a localized defect applying piecewise response function, *Mechanism and Machine Theory*, 56 (2012) 156-169.
[19] M. Cheikh, S. Quilici and G. Cailletaud, Presentation of KICOF, a phenomenological model of variable friction in fretting contact, *Wear*, 119 (2007) 15-19.
[20] J. Besson and R. Foerch, Object-oriented programming applied to the finite element method. part I: General concepts, *Revue Européenne des Eléments Finis*, 70 (1998) 535-566.
[21] A. B. Jones, A general theory for elastically constrained ball and radial roller bearings under arbitrary load and speed conditions, *Trans. ASME*, 82 (1) (1960) 309-320.
[22] N. T. Liao and J. F. Lin, Ball bearing skidding under radial and axial loads, *Mechanism and Machine Theory*, 37 (1) (2002) 91-113.
[23] L. Mi, G. F. Yin, M. N. Sun and X. H. Wang, Effects of preloads on joints on dynamic stiffness of a whole machine tool structure, *Journal of Mechanical Science and Technology*, 26 (2) (2012) 495-508.
[24] T. Tao X. Mei, M. Tsutsumi and N. Sun, Study on load distribution of ball screws with errors, *Mechanism and Machine Theory*, 38 (2001) 1257-1269.
[25] Rashad A. Abdel-Baky and Reem A. Al-Ghefari, On the kinematic geometry of relative screw motions. *Journal of Mechanical Science and Technology*, 26 (8) (2012) 2497-2503.
[26] Y. Barranger, R. Bertolaso, P. Doumalin, J. C. Dupré, A. Germaneau, and M. Cheikh. Experimental validation of a numerical simulation on a ball-screw system by 3D photoelasticity, *EPJWebof Conferences6*, Poitiers, France (2010) DOI:10.1051/epjconf/20100632003.

Mohammed Cheikh received his thesis (Ph.D.) from the University of Bourgogne (France) in 1997. He is currently an assistant professor at the University of Toulouse (IUT Figeac and Ecole des Mines Albi). His research interests are fretting and wear by numerical and experimental approaches.

Arnaud Germaneau received his Ph.D. from the University of Poitiers in 2007. Dr. Germaneau is currently an assistant Professor at the University of Poitiers in the PPRIME Institute. His research interests include experimental mechanics, photomechanics, mechanical analysis of structures and materials, and model validation/identification.

Pascal Doumalin received his thesis (Ph.D.) from Ecole Polytechnique (France) in 1999. He is currently an assistant professor at the University of Poitiers. His research interests concern the study of mechanical behaviour of materials and structures by using non-contact measurement methods.

Jean-Christophe Dupré received his Ph.D. from the University of Poitiers in 1992. Dr. Dupré is CNRS Researcher at the Institute PPRIME in the Team PEM (Photomechanics and Experimental Mechanics), University of Poitiers. His research interests include the development of optical methods, 2D and 3D.